IEEE INSTRUMENTATION & MEASUREMENT SOCIETY

Received 29 May 2022; revised 24 July 2022; accepted 2 August 2022. Date of publication 15 August 2022; date of current version 30 August 2022.
The review of this article was arranged by Associate Editor Wuqiang Yang.

Digital Object Identifier 10.1109/OJIM.2022.3198476

Multiple Regression Fitting Electrical Impedance Spectro-Tomography for Quantitative Image Reconstruction of Dead Cell Fraction and Cell Concentration

DAISUKE KAWASHIMA [1], HIROMICHI OBARA [2], AND MASAHIRO TAKEI [3] (Member, IEEE)

[1] Institute for Advanced Academic Research and Graduate School of Engineering, Chiba University, Chiba 2638522, Japan
[2] Department of Mechanical System Engineering, Tokyo Metropolitan University, Tokyo 1910065, Japan
[3] Graduate School of Engineering, Chiba University, Chiba 2638522, Japan

CORRESPONDING AUTHOR: H. OBARA (e-mail: obara@tmu.ac.jp)

This work was supported by JSPS KAKENHI under Grant JP19J00240 and Grant JP21K14072.

ABSTRACT A novel image reconstruction method called multiple regression fitting electrical impedance spectro-tomography (*mrf*-EIST) has been proposed in order to realize the quantitative image reconstruction of dead cell fraction ϕ_d and cell concentration c_c in a huge amount of cell environment. *mrf*-EIST statistically selects frequencies to extract two variables ψ_d and ψ_c, which quantifyϕ_d and c_c, respectively. The ϕ_d and c_c images are reconstructed by solving the inverse problem using ψ_d and ψ_c. To validate the performance of *mrf*-EIST, the image reconstruction by *mrf*-EIST in the frequency range from 100 Hz to 1 MHz is carried out under the condition that the number of cells is over 10^9 cells. As a result, *mrf*-EIST shows that the image quality defined by the difference in pixel value from the true image is less than 0.050 in ϕ_d and 0.071 in c_c, respectively. In comparison to frequency-difference EIT (*fd*-EIT) as a conventional EIST regarding a position error of center of gravity, *mrf*-EIST provides much more accurate images, qualitatively and quantitatively, compared to the *fd*-EIT.

INDEX TERMS Electrical impedance spectro-tomography, multiple regression fitting, dead cell fraction, cell concentration.

I. INTRODUCTION

Cell imaging plays an extremely beneficial role for cell condition observation under cell culturing and cell differentiation of pluripotent stem cells for cell manufacturing, e.g., organogenesis. For an application of cell manufacturing, a non-invasive cell imaging is essential to estimate cell conditions such as dead cell fraction and cell concentration in a huge amount of cell environment over one billion cells. As a conventional invasive imaging technique, electrochemical imaging (ECI) was utilized [1], [2], [3], [4]. ECI applies electrochemical reactions such as redox reaction using micro- or nano-sized electrode probe to measure pA order current [5]. Although ECI is useful for analysing the mass exchange between cells and extracellular liquid, ECI does not reflect the cell itself. Also, ECI is not applicable in a huge amount of cell environment.

For an imaging technique under a huge amount of cell environment, electrical impedance tomography (EIT) has been currently paid attention [6], [7]. EIT visualizes the cross-sectional image reconstructed by solving an inverse problem using impedance which is measured at the multiple combinations of electrodes around the region of interest. Sun *et al.* [8] and Yang *et al.* [9] fabricated a miniature electrode sensor to apply EIT to cell imaging. They successfully reconstructed the conductivity distribution of cells and tissues. Although EIT has a possibility to provide the information regarding dead cell fraction and cell concentration in a huge amount of cell environment, the reconstructed image by EIT generally represents conductivity and permittivity distributions. Even though conductivity and permittivity can reflect cell conditions, i.e., dead cell fraction and cell concentration, the reconstructed image was applicable only for shape recognition and location detection of cells and tissues [7], [8]. To provide dead cell fraction and cell concentration, the spectral analysis, i.e., electrical impedance spectroscopy (EIS) which analyses the electrical characteristics of cells is necessary [10], [11], [12].

Currently, the electrical impedance spectro-tomography (EIST) was developed [13], [14], [15], [16] to combine EIT with EIS. A typical EIST applies the impedance difference at two different frequencies to the EIT image reconstruction algorithm, called as frequency different EIT (*fd*-EIT) [17]. Although *fd*-EIT estimated several tissue locations, dead cell fraction and cell concentration in a huge amount of cell environment cannot be quantified. Thus, it is still challenging to reconstruct the quantitative image of dead cell fraction and cell concentration in a huge amount of cell environment. Also, frequencies applied to the image reconstruction on the conventional EIST was not reasonable because frequencies were arbitrarily selected that the reconstructed image resembles the model set by the researcher's subjectivity [16], [18], [19]. To realize the quantitative image reconstruction, a reasonable frequency selection through an electrical impedance spectral analysis is essential for the image reconstruction by EIST.

Therefore, this study proposes a novel image reconstruction method using the multiple regression fitting EIST (*mrf*-EIST) to realize a quantitative image reconstruction of dead cell fraction and cell concentration in a huge amount of cell environment. The *mrf*-EIST statistically selects suitable frequencies to obtain two variables which quantify dead cell fraction and cell concentration, respectively. Image reconstruction is carried out using the two variables to visualize and quantify the dead cell fraction and cell concentration under the condition that the number of cells is over 10^9 cells. To evaluate *mrf*-EIST, *fd*-EIT is also applied as a conventional image reconstruction of EIST to compare with *mrf*-EIST.

II. METHODOLOGY

A. OVERVIEW OF MRF-EIST

The proposed *mrf*-EIST which reconstructs images of dead cell fraction ϕ_d and cell concentration c_c is constructed of two parts: (I) stepwise regression and (II) image reconstruction as shown in Fig. 1. The *mrf*-EIST

In stepwise regression part (I), the stepwise regression (SWR) as one of the multiple regression fittings is performed to extract two variables ψ_d and ψ_c which quantify ϕ_d and c_c, respectively from measured impedance data. In this study, we chose SWR instead of other representative regression methods such as principal component regression (PCR) and the Lasso regularization. PCR induces low prediction accuracy due to a variable composition from the explanatory variables [20]. Lasso regularization induces the

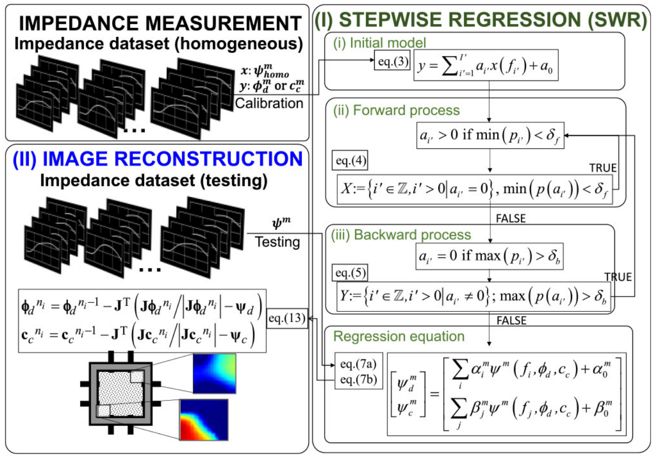

FIGURE 1. Overview of the proposed *mrf*-EIST.

dense model using a relatively large number of explanatory variables if the variables are corelated [21].

In image reconstruction part (II), ϕ_d and c_c images are reconstructed using $\boldsymbol{\psi}_d$ and $\boldsymbol{\psi}_c$ as observation vector of ψ_d and ψ_c instead of impedance based on EIT algorithm. Here, ϕ_d is defined as the fraction of dead cell volume to total cell volume and c_c is as the fraction of total cell volume to total volume of cell suspension.

Note that although SWR is employed as a linear multiple regression, any multiple regressions can be applicable such as PCR, Lasso regularization and any other regressions. The key technology to this study is to extract new variables reflecting the target value from measured impedance to be employed as the observation vector in the inverse problem of image reconstruction.

B. STEPWISE REGRESSION FITTING

For the preprocessing by the SWR fitting, an input dataset is prepared from impedance measurement data. Impedance is measured as complex value from multiple electrode combinations as shown in Fig. 2 (c) (described later in Chapter III). As an input dataset, we employed the normalized reactance ψ which depends on complex permittivity (including permittivity and conductivity) of cell suspension (see the Appendix) because ψ highly reflects the dead cell fraction ϕ_d according to our previous study [11]. When impedance is measured at the m-th electrode combination ($m = 1, 2, \ldots, M$) expressed by Z^m, ψ^m is calculated by

$$\psi^m(f, \phi_d, c_c) = 1 - \frac{Z''^m(f, \phi_d, c_c)}{Z''^m_{homo}\left(f, \phi_d^0, c_c^0\right)} \tag{1}$$

where Z'' is reactance, M is the total number of combination and the superscript 0 represents a reference value. Z''^m_{homo} represents the reactance under the condition that both ϕ_d and c_c are homogeneously distributed, which is used as a baseline of the normalization. As described in eq. (1), ψ^m is a function of ϕ_d and c_c as well as frequency f.

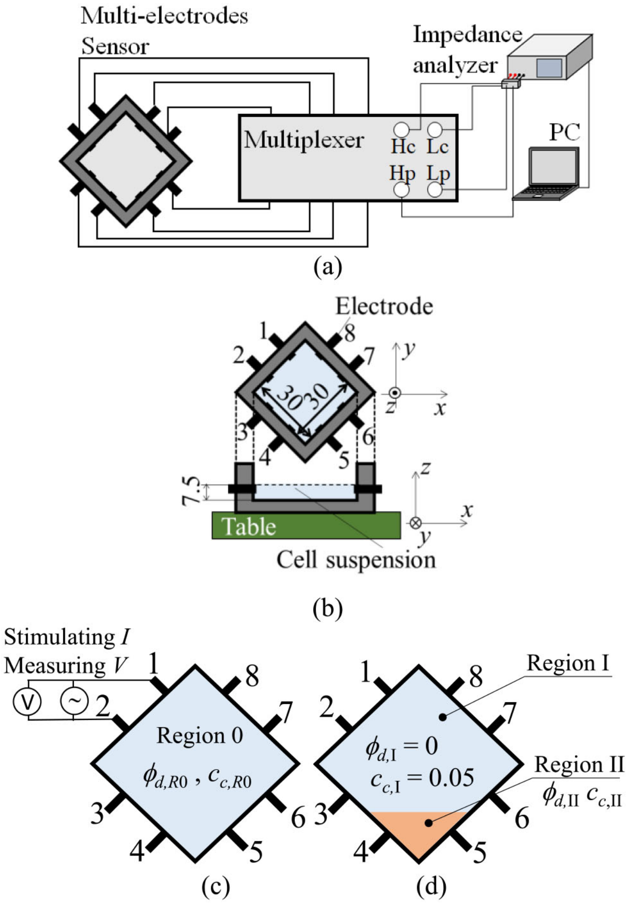

FIGURE 2. (a) Schematic of experimental setup. (b) The size of the multi-electrodes sensor. The unit of length is mm. (c) and (d) shows experimental conditions. (c) Homogeneous conditions in which calibration was conducted. (d) Inhomogeneous conditions.

For a calibration, the SWR fitting is conducted using ψ''^{m}_{homo} under homogeneous distribution of ϕ_d and c_c described as

$$\psi^{m}_{homo}(f, \phi_d, c_c) = 1 - \frac{Z''^{m}_{homo}(f, \phi_d, c_c)}{Z''^{m}_{homo}\left(f, \phi^0_d, c^0_c\right)} \tag{2}$$

This study employs the bidirectional elimination in SWR [22]. The SWR is carried out by following three processes.

(i) Initial model: The model of the regression equation is described by a multiple linear equation as follows:

$$y = \sum_{i'=1}^{I'} a_{i'} x(f_{i'}) + a_0 \tag{3}$$

where x is an explanatory variable which is ψ''^{m}_{homo} as a function of f, y is an objective variable which represents ϕ_d or c_c and a is a coefficient of explanatory variables. Subscript i' denotes the numbering of frequency, and I' is the total number of sweeping frequencies. Initially, the regression equation starts from a constant model which includes only an intercept a_0, while the other coefficients $a_{i'} = 0$. If some characteristic frequencies are already known, it is better to add the variables at those frequencies to the initial equation. To solve the multiple linear equation eq. (3) is solved by QR decomposition [23].

(ii) Forward process: The regression equation is updated based on p-value of F static which is calculated from $a_{i'}$ in order to pick up a new variable $x(f_{i'})$ at another frequency. The p-value is calculated from each coefficient $a_{i'}$, where $p(a_{i'})$ denotes p-value of $a_{i'}$. In order to search a variable which is employed in the regression equation, each variable among $a_{i'}$ is individually added to the regression equation to obtain p-value (e.g., if the current equation is $y = a_0$, try $y = a_1x_1 + a_0$, $y = a_2x_2 + a_0$, $\ldots$, $y = a_{I'}x_{I'} + a_0$, respectively). The p-value indicates the significance of the coefficient $a_{i'}$, which is obtained from the F distribution [24]. Among them, a variable for which proposition (3) is true is employed to the model.

$$X := \left\{ i' \in \mathbb{Z}, i' > 0 \middle| a_{i'} = 0 \right\}, \min(p(a_{i'})) < \delta_f \tag{4}$$

A tolerance $\delta_f = 0.05$ as a general value is used [25]. This procedure is repeated until proposition (4) becomes false.

(iii) Backward process: The updated equation is revised by eliminating variable $x(f_{i'})$ while proposition (5) is true.

$$Y := \left\{ i' \in \mathbb{Z}, i' > 0 \middle| a_{i'} \neq 0 \right\}; \max(p(a_{i'})) > \delta_b \tag{5}$$

Generally, 0.10 is used as a tolerance δ_b [25]. If proposition (5) is false, the process is finished.

Finally, linear equations are obtained using ψ, the estimated ϕ_d and c_c instead of x and y as follows:

$$\phi_{d,est} = \sum_{i=1}^{I} \alpha_i \psi_{homo}(f_i, \phi_d, c_c) + \alpha_0 \tag{6a}$$

$$c_{c,est} = \sum_{j=1}^{J} \beta_i \psi_{homo}(f_i, \phi_d, c_c) + \beta_0 \tag{6b}$$

where $\phi_{d,est}$ and $c_{c,est}$ are the estimated ϕ_d and c_c, α and β are coefficients or intercepts. i and j represent the selected frequency by SWR.

C. IMAGE RECONSTRUCTION

ϕ_d and c_c are reconstructed using ψ^m_d and ψ^m_c obtained from ψ. Eqs. (6a) and (6b) can be modified using ψ^m_d and ψ^m_c instead of $\phi^m_{d,est}$ and $c^m_{c,est}$ as follows:

$$\psi^m_d = \sum_{i=1}^{I} \alpha^m_i \psi^m(f_i, \phi_d, c_c) + \alpha^m_0 \tag{7a}$$

$$\psi^m_c = \sum_{j=1}^{J} \beta^m_j \psi^m\left(f_j, \phi_d, c_c\right) + \beta^m_0 \tag{7b}$$

Instead of resistance or reactance which is conventionally applied to the image reconstruction in EIST, ψ_d and ψ_c are applied to the image reconstruction. The linear relationship between ψ_d and ϕ_d or ψ_c and c_c is assumed as follows:

$$\boldsymbol{\psi}_d = \mathbf{J}\boldsymbol{\phi}_d \tag{8}$$
$$\boldsymbol{\psi}_c = \mathbf{J}\mathbf{c}_c \tag{9}$$

where $\boldsymbol{\psi}_d$ and $\boldsymbol{\psi}_c$ are the observation vectors using the reactance written by

$$\boldsymbol{\psi}_d = \left[\, \psi_d^1 \; \psi_d^2 \cdots \psi_d^m \cdots \psi_d^{M-1} \; \psi_d^M \,\right]^{\mathrm{T}} \tag{10}$$
$$\boldsymbol{\psi}_c = \left[\, \psi_c^1 \; \psi_c^2 \cdots \psi_c^m \cdots \psi_c^{M-1} \; \psi_c^M \,\right]^{\mathrm{T}} \tag{11}$$

$\boldsymbol{\phi}_d \in \mathbb{R}^N$ and $\mathbf{c}_c \in \mathbb{R}^N$ are the column vectors of the distributions of ϕ_d and c_c, respectively. N represents the number of elements in reconstructed image. $\mathbf{J} \in \mathbb{R}^{M\times N}$ is a normalized Jacobian. In the case of two-terminal mode [11], $\mathbf{J}$ is calculated by

$$\mathbf{J} = \left[\, \mathbf{j}^1 \; \mathbf{j}^2 \cdots \mathbf{j}^n \cdots \mathbf{j}^{N-1} \; \mathbf{j}^N \,\right] \tag{12a}$$
$$\mathbf{j}^n = \left[\, \frac{j'^{1,n}}{\sum_m j'^{m,n}} \; \frac{j'^{2,n}}{\sum_m j'^{m,n}} \cdots \frac{j'^{m,n}}{\sum_m j'^{m,n}} \cdots \frac{j'^{M-1,n}}{\sum_m j'^{m,n}} \; \frac{j'^{M,n}}{\sum_m j'^{m,n}} \,\right]^T \tag{12b}$$
$$j'^{m,n} = \int_{\Omega_n} -\nabla\, v^{m,n}\left(\varepsilon_0^*\right) \cdot \nabla\, v^{m,n}\left(\varepsilon_0^*\right)\, \mathrm{d}\Omega \tag{12c}$$

where v is potential and Ω_n is the area at a pixel n (= 1, 2, ..., N). j' is an element of Jacobian which is obtained by the same procedure in [26]. Complex permittivity $\varepsilon_0{}^*$ of water at 25 ℃ was used for the calculation of j'. To obtain the potential distribution v in eq. (12c) for the Jacobian calculation, AC/DC module in the COMSOL Multiphysics software (version 5.3a) was used.

For the inverse solutions of $\boldsymbol{\phi}_d$ and $\mathbf{c}_c$ in eqs. (8) and (9), the iterative algorithm was utilized because the inverse problem in EIT is in ill-posed condition [27]. In this paper, we applied the GVSPM algorithm [28] defined as

$$\begin{aligned} \boldsymbol{\phi}_d^{n_i} &= \boldsymbol{\phi}_d^{n_i-1} - \mathbf{J}^{\mathrm{T}}\left(\frac{\mathbf{J}\boldsymbol{\phi}_d^{n_i-1}}{\left|\mathbf{J}\boldsymbol{\phi}_d^{n_i-1}\right|} - \boldsymbol{\psi}_d\right) \\ \mathbf{c}_c^{n_i} &= \mathbf{c}_c^{n_i-1} - \mathbf{J}^{\mathrm{T}}\left(\frac{\mathbf{J}\mathbf{c}_c^{n_i-1}}{\left|\mathbf{J}\mathbf{c}_c^{n_i-1}\right|} - \boldsymbol{\psi}_c\right) \end{aligned} \tag{13}$$

where n_i is an iterative number.

III. EXPERIMENT

A. EXPERIMENTAL SETUP

Fig. 2 shows an experimental setup which consisted of a multi-electrode sensor, a multiplexer, an impedance analyzer (IM3570, HIOKI, Japan) and a PC. The multi-electrodes sensor had a square-shaped cage with eight electrodes which were stainless steel screw with 5.0 mm in diameter. Each electrode was connected to the multiplexer to switch the combination of electrodes to measure impedance by the impedance analyzer. Four ports of the impedance analyzer which are Hc, Lc, Hp and Lp were connected to the corresponding ports on the multiplexer. In the multiplexer, Hc and Hp ports and Lc and Lp ports were combined respectively in order to realize two-terminal mode, which injected current and measured voltage at the same electrode combination. The PC controlled the measurement system and accumulated all experimental data in its storage.

B. EXPERIMENTAL METHOD

A fixed current at 10 μA was stimulated at the combination of k-th and l-th electrodes ($k < l$, $\max(k) = K = L - 1$ and $\max(l) = L$), and voltage was measured at the same electrode combination. Since this study employed 8 electrodes, $K = 7$ and $L = 8$. The total number of electrode combination $M = 28$.

Cell suspension was injected in the sensor with the height $h = 7.5$ mm. To make the coefficients α and β by SWR, the homogeneous distributions of ϕ_d and c_c were applied as shown in Fig. 2 (c) (Case 1). For the validation of the proposed image reconstruction, inhomogeneous distributions were applied as shown in Fig. 2 (d) (Case 2). To construct the distributions as shown in Fig. 2 (d), we injected the cell suspension in separated regions by a partition plate. After cell sedimentation, the partition plate was removed, and then the impedance measurement was started.

C. EXPERIMENTAL CONDITIONS

In the case of homogeneous distributions (Case 1), cell suspension was homogeneously distributed in the sensor under the fixed $\phi_{d,0}$ and $c_{c,0}$ in Region 0 as shown in Fig. 2 (c). We prepared 59 samples under the conditions of $\phi_{d,R0}$ (6 conditions) and $c_{c,R0}$ (3 conditions) combinations, which included 41 samples for calibration and the remained 18 samples for testing. c_c = 0.05, 0.08 and 0.10 which were measured by a capillary tube centrifuge system (Micro hematocrit Centrifuge Model 3220; Kubota Corporation, Tokyo, Japan) were converted into 5.16×10^9, 8.25×10^9 and 10.3×10^9 cells in the number of cells in the multi-electrode sensor (6.75 mL in total volume of cell suspension) under the assumption that the cell size was 5 μm in diameter. In the case of inhomogeneous distributions (Case2), the sensor area was divided into two regions: Region I and Region II as shown in Fig. 2 (d). In Region I, $\phi_{d,\mathrm{I}}$ and $c_{c,\mathrm{I}}$ were fixed at $\phi_{d,\mathrm{I}} = 0$ and $c_{c,\mathrm{I}} = 0.05$, respectively. In Region II, $\phi_{d,\mathrm{II}}$ and $c_{c,\mathrm{II}}$ were changed in each condition (detail conditions are listed in Fig. 5).

This study used yeast cell suspension. Cell suspensions with ϕ_d and c_c were prepared by the following procedure. Firstly, yeast cells were cultured in a distilled water for 30 min at fixed water temperature T_w = 298 K. To make dead cell suspension, living cells were kept in hot water at temperature T_w = 363 K for 5 min in order to artificially destroy the plasma membrane. Note that dead cell keeps its shape and volume even though the membrane is destructed because yeast cell has a cell wall, which is maintained after heat treatment. After c_c of living and dead cells was temporally measured, c_c was adjusted by the amount of distilled water. In order to make a cell suspension with the fixed ϕ_d, the living cell suspension and the dead cell suspension were mixed.

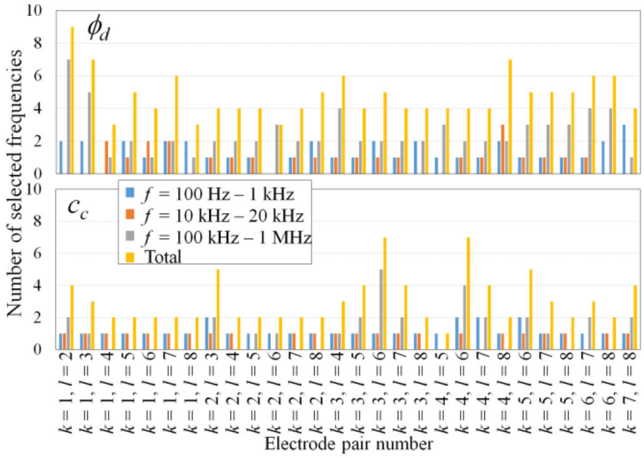

FIGURE 3. The number of frequencies selected through the stepwise fitting.

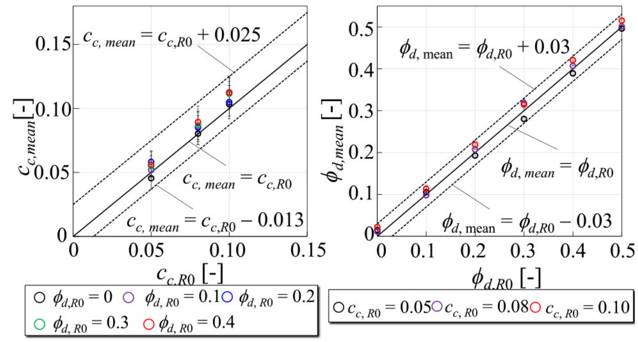

(a) (b)

FIGURE 4. Spatial mean value of (a) $\phi_{d,\,mean}$ and (b) $c_{c,\,mean}$ against each controlled value $c_{c,R0}$ and $\phi_{d,R0}$.

IV. RESULTS

A. CASE 1 HOMOGENEOUS DISTRIBUTION

By SWR fitting, the regression coefficients α_i and β_j at selected frequencies were obtained. Fig. 3 shows the number of frequencies in three frequency ranges (f = 100 Hz to 1000 Hz, 10 kHz to 20 kHz, and 100 kHz to 1 MHz) selected by SWR in the case of ϕ_d (upper) and c_c (bottom). In the most cases, three to five different frequencies suitable for image reconstruction of ϕ_d and two to four ones for c_c were selected by SWR. The selected frequencies were included in the frequency ranges of 100 Hz to 1000 Hz, 10 kHz to 20 kHz, and 100 kHz to 1 MHz. Note that although we applied SWR to all electrode combinations, ideally it is sufficient to apply SWR to a single electrode combination. However, technically we can consider applying SWR to all electrode combination in order to compensate the electrical characteristics of each individual electrode.

Image reconstruction of $\boldsymbol{\phi}_d$ and $\mathbf{c}_c$ was carried out using ψ_d^m and ψ_c^m obtained from ψ_{homo}^m by eq. (7a) and (7b) based on SWR. For the quantitative evaluation of $\boldsymbol{\phi}_d$ and $\mathbf{c}_c$, the spatial mean values of $\boldsymbol{\phi}_d$ and $\mathbf{c}_c$ were used. Fig. 4 shows (a) the spatial mean value of $\boldsymbol{\phi}_d$, $\phi_{d,mean}$ against $\phi_{d,R0}$ and (b) the spatial mean value of $\mathbf{c}_c$, $c_{c,mean}$

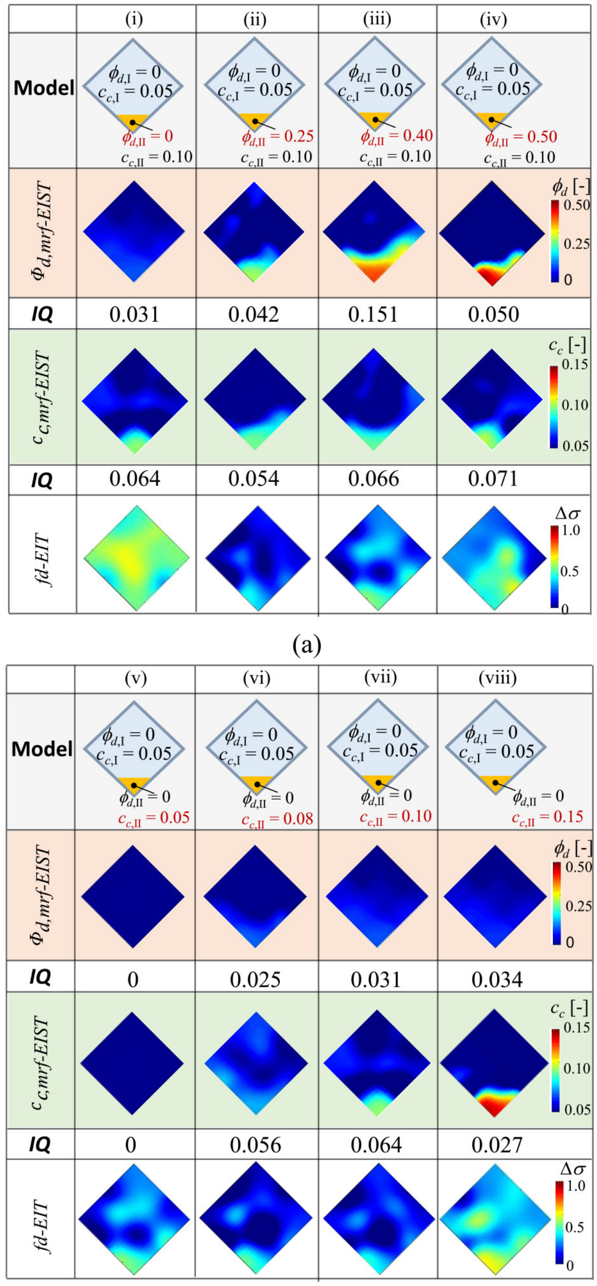

(a)

(b)

FIGURE 5. Reconstructed image of ϕ_d and c_c by *mrf*-EIST under (a) fixed $c_{c,\text{II}}$ and (b) fixed $\phi_{d,\text{II}}$ in Region II shown in Fig. 2 (d). Images reconstructed by *fd*-EIT are also shown at f_a = 1.6 kHz and f_b = 31 kHz.

against $c_{c,R0}$. $\phi_{d,mean}$ and $c_{c,mean}$ became slightly bigger with increasing $\phi_{d,R0}$ and $c_{c,R0}$, respectively. In this measurement range, $\phi_{d,mean}$ was measured within ± 0.03 and $c_{c,mean}$ was within +0.025 and −0.013 in absolute error, respectively.

B. CASE 2 INHOMOGENEOUS DISTRIBUTION

Image reconstruction was carried out in the inhomogeneous case (Case2) using the same regression coefficients α and β obtained in the homogeneous case (Case 1). In Case 2, $\phi_{d,\text{II}}$ or $c_{c,\text{II}}$ in Region II was changed, while the other value was fixed. Fig. 5 shows the reconstructed images

TABLE 1. Experimental condition.

Case 1: Homogeneous			
	Parameter	Symbol	Calibration/Testing
Region 0	Dead cell fraction	$\phi_{d,R0}$ [-]	0
			0.1
			0.2
			0.3
			0.4
			0.5
	Cell concentration	$c_{c,R0}$ [-]	0.05
			0.08
			0.10

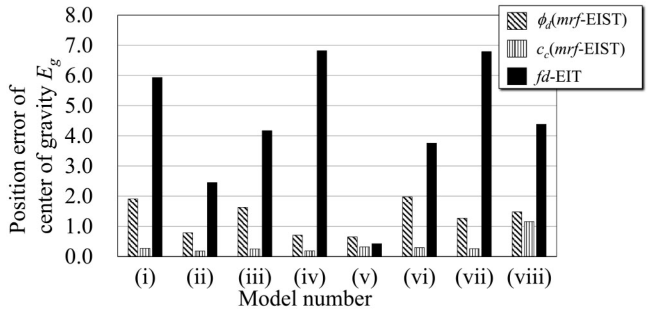

FIGURE 6. Position error of a center of gravity coordinate E_r at each condition in comparison to *mrf*-EIST and *fd*-EIT.

of (a) ϕ_d and (b) c_c, which were represented by $\phi_{d,mrf-EIST}$, and $c_{c,mrf-EIST}$, respectively. According to Fig. 5 (a) under fixed $c_{c,\mathrm{II}}$ in Region II, $\phi_{d,mrf-EIST}$ was changed in the bottom section, while $c_{c,mrf-EIST}$ was almost homogeneously distributed at $c_c = 0.01$. In contrast, Fig. 5 (b) shows that $c_{c,mrf-EIST}$ was changed in the bottom section, while $\phi_{d,mrf-EIST}$ was homogeneously distributed at $\phi_d = 0$ under fixed $\phi_{d,\mathrm{II}}$ in Region II.

The reconstructed images were evaluated by the image quality defined by

$$IQ = \frac{\sum_{n=1}^{N} \sqrt{\left(F^n_{mrf-EIST} - F^n_{model}\right)^2}}{N} \tag{14}$$

where F represents ϕ_d or c_c, $n \in \mathbb{R}^N$ is pixel number and N is the total number of pixels. The subscript *model* represents the model image shown in Fig. 5. Fig. 5 also shows IQ of each condition, which shows that the reconstructed image by *mrf*-EIST had agreement with the original distribution (in Table 1) within max $IQ < 0.050$ in $\phi_{d,mrf-EIST}$ and within max $IQ < 0.071$ in $c_{c,mrf-EIST}$. For ϕ_d, the accuracy was 80 %, which was roughly calculated by $\left(1 - IQ/\phi_{d,model}\right) \times 100$. Although the accuracy of the *mrf*-EIST is inferior to a conventional trypan blue dying imaging with from 85 % to 95 % in accuracy [29], the accuracy is able to be improved by statistical model instead of SWR such as Lasso and Bayesian inferences.

Fig. 5 also shows the reconstructed images by *fd*-EIT calculated using the following equation.

$$\Delta\boldsymbol{\sigma}^{n_i} = \Delta\boldsymbol{\sigma}^{n_i - 1} - \mathbf{J}^{\mathrm{T}}\left(\frac{\mathbf{J}\Delta\boldsymbol{\sigma}^{n_i}}{|\mathbf{J}\Delta\boldsymbol{\sigma}^{n_i}|} - \Delta\mathbf{Z}\right) \tag{15}$$

where $\Delta\mathbf{Z}$ denotes the resistance difference at two different frequencies f_a and f_b ($f_a < f_b$). According to preliminary experiments, we chose $f_a = 1.6$ kHz and $f_b = 31$ kHz, at which impedance difference shows better image. The same image reconstruction algorithm (GVSPM) was used. Although *fd*-EIT visualized the bottom section's location, *fd*-EIT showed many image artifacts and does not show quantitative images of ϕ_d or c_c.

To evaluate the spatial distribution of the bottom region, we obtained a position error of a center of gravity coordinate E_g of bottom region calculated by following equation.

$$E_g = \sqrt{\left(x_g - x_{g,model}\right)^2 - \left(y_g - y_{g,model}\right)^2} \tag{16}$$

where a center of gravity coordinate (x_g, y_g) was calculated by

$$x_g = \sum_{m=1}^{MN} F(m)x(m) \tag{17}$$

$$y_g = \sum_{m=1}^{MN} F(m)y(m) \tag{18}$$

F represents ϕ_d, c_c or $\Delta\sigma$ obtained from Fig. 5. The x and y represent the position coordinate at each pixel. Likewise, a center of gravity coordinate of a model ($x_{g,model}$, $y_{g,model}$) as a true value was calculated.

Fig. 6 shows E_g at each condition. In comparison to *fd*-EIT, E_g of *mrf*-EIST was much lower. In the average of E_g under all conditions, $E_g = 1.30 \pm 0.536$ mm in ϕ_d (*mrf*-EIST), $E_g = 0.36 \pm 0.323$ mm in c_c (*mrf*-EIST) and $E_g = 4.34 \pm 2.202$ mm in *fd*-EIT, which indicated the accuracy of a position estimation by *mrf*-EIST was more accurate than that by the *fd*-EIT. Also, it is difficult to quantitatively estimate ϕ_d and c_c by *fd*-EIT. In contrast, the *mrf*-EIST provided better images of ϕ_d and c_c, qualitatively and quantitatively.

V. DISCUSSION

In order to realize a quantitative image reconstruction of ϕ_d and c_c by *mrf*-EIST, a unique spectral characteristic of relative permittivity ε_r and conductivity σ of cell suspension by fluctuations of ϕ_d and c_c are required. We also measured ε_r and σ spectra in the frequency range from 100 Hz to 1 MHz using a cuvette with two parallel plate electrodes (2.0 mm in electrode gap and 200 mm^2 in electrode surface area) (Model EC-002S, Nepa Gene E.E Corporation, Japan) and the impedance analyzer (IM3570, HIOKI, Japan) system [11].

Fig. 7 (a) shows ε_r and σ spectral changes by ϕ_d at $c_c = 0.05$ and (b) changes by c_c at $\phi_d = 0$. ε_r was decreased with increasing f due to dielectric relaxation by the plasma membrane ($f \approx 100$ kHz) and electrical double layer ($f \approx 1$ kHz) [30]. ε_r was slightly changed by ϕ_d and

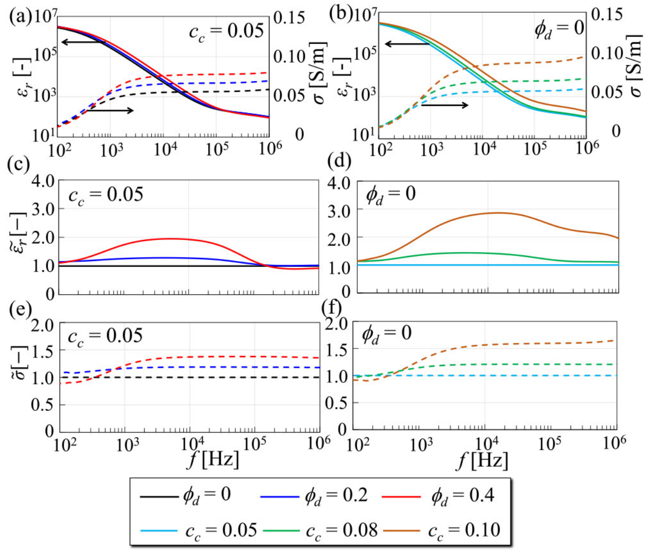

FIGURE 7. Spectral variation of relative permittivity ε_r and conductivity σ by (a) ϕ_d at $c_c = 0.05$ and (b) c_c at $\phi_d = 0$. Spectral variation of $\widetilde{\varepsilon_r}$ by (c) ϕ_d at $c_c = 0.05$ and (d) c_c at $\phi_d = 0$ and that of $\tilde{\sigma}$ by (e) ϕ_d at $c_c = 0.05$ and (f) c_c at $\phi_d = 0$.

c_c, while σ became significantly larger with increasing ϕ_d and c_c, which can reflect the conductivity variation in the medium of cell suspension.

To make the difference in ε_r and σ clear, $\widetilde{\varepsilon_r} = \varepsilon_r/\varepsilon_{r,ref}$ and $\tilde{\sigma} = \sigma/\sigma_{ref}$ are also useful because ψ is described by the both ratios (see the Appendix). Fig. 7 (c) and (d) show spectral change in $\widetilde{\varepsilon_r}$ by ϕ_d and c_c, respectively. A broad peak in $\widetilde{\varepsilon_r}$ around 10 kHz due to changing in ϕ_d and two peaks at 10 kHz and 700 kHz due to change in c_c. The peak at $f = 10$ kHz reflects the condition of medium in which the concentration of ions or some other conductive materials released from cells varied due to the changes in ϕ_d and c_c [11]. The peak at $f = 700$ kHz reflected the number of cells because cells have plasma membrane which plays a role of capacitor. Also, the effect of the number of dielectric particles were observed in Fig. 7 (c). If the number of dead cells is increased which means ϕ_d is increased, the dielectric particles are decreased because the plasma membrane as dielectric material is ruptured in dead cell. As shown in Fig. 7 (d), ε_r at $f = 700$ kHz is slightly decreased with increasing ϕ_d. As shown in Fig. 7 (e) and (f), $\tilde{\sigma}$ was similarly changed by both ϕ_d and c_c, which indicated that the conductivity mainly reflected the medium condition. Thus, ε_r and σ show the unique spectral characteristics due to the differences in the number of dielectric particles and the medium difference according to the variations of ϕ_d and c_c. If more factors such as cell species and other biological conditions are involved, other frequencies are necessary. Although in this study, we did not consider the resistance because of the multicollinearity which leads to the overfitting, the resistance as well as reactance is also a candidate as an explanatory variable in the regression equation in order to extract the multiple factors.

VI. CONCLUSION

This study proposed a novel image reconstruction method using the multiple regression fitting EIST (*mrf*-EIST) in order to realize a quantitative image reconstruction of dead cell fraction and cell concentration in a huge amount of cell environment. The *mrf*-EIST applies a stepwise regression as a multiple regression fitting to electrical impedance spectra in order to extract two variables which quantify dead cell fraction and cell concentration, respectively. By using the two variables, the reconstructed images of ϕ_d and c_c were obtained. The details are as follows:

1) Three to five different frequencies suitable for image reconstruction of ϕ_d and two to four frequencies for c_c were selected through the stepwise regression. The selected frequencies were in three frequency ranges of 100 Hz to 1000 Hz, 10 kHz to 20 kHz, and 100 kHz to 1 MHz.
3) In the case of homogeneous distribution, *mrf*-EIST successfully reconstructed the ϕ_d and c_c images. Their spatial mean values $\phi_{d,mean}$ and $c_{c,mean}$ showed agreement with the controlled values $\phi_{d,ctrl}$ within $\pm$ 0.02 and $c_{c,ctrl}$ within +0.025 and −0.012.
3) In the case of inhomogeneous distribution, *mrf*-EIST showed the image quality IQ of $\phi_{d,mrf-EIST}$ was less than 0.050 and IQ of $c_{c,mrfEIST}$ was less than 0.071 in a range of the number of cells 5.16×10^9 to 10.3×10^9 cells. In comparison to *fd*-EIT, the *mrf*-EIST showed much better accuracy regarding a position error of center of gravity E_g such as $E_g = 1.30 \pm 0.536$ mm in ϕ_d (*mrf*-EIST) and $E_g = 0.36 \pm 0.323$ mm in c_c (*mrf*-EIST), which were much less than $E_g = 4.34 \pm 2.202$ mm in *fd*-EIT.

APPENDIX

The complex impedance, Z^* between two parallel electrodes (electrode gap L_e and electrode surface area A_e) where a material with relative permittivity ε_r and conductivity σ is written as

$$Z^* = \frac{1}{\sigma K + j\omega\varepsilon_0\varepsilon_r K} = \frac{\sigma - j\omega\varepsilon_0\varepsilon_r}{\sigma^2 + (\omega\varepsilon_0\varepsilon_r)^2}\frac{1}{K} \tag{A1}$$

where K ($=A_e/L_e$) is a configuration parameter of the electrode. ψ is written as follows:

$$\begin{aligned}\psi &= 1 - \frac{Z''(\phi, c)}{Z''(\phi_{ref}, c_{ref})} \\ &= 1 - \frac{\frac{\omega\varepsilon_0\varepsilon_r}{\sigma^2+(\omega\varepsilon_0\varepsilon_r)^2}}{\frac{\omega\varepsilon_0\varepsilon_{r,ref}}{\sigma_{ref}^2+(\omega\varepsilon_0\varepsilon_{r,ref})^2}} \\ &= 1 - \frac{\varepsilon_r}{\varepsilon_{r,ref}}\frac{\sigma_{\text{ref}}^2 + (\omega\varepsilon_0\varepsilon_{r,\text{ref}})^2}{\sigma^2 + (\omega\varepsilon_0\varepsilon_r)^2}\end{aligned} \tag{A2}$$

where subscript *ref* represents a reference condition. In the case that $^2 \gg (\omega\varepsilon_0\varepsilon_r)^2$ can be consistent at low f, eq. (A2) is rewritten as

$$\psi \approx 1 - \frac{\sigma_{ref}^2}{\sigma^2}\frac{\varepsilon_r}{\varepsilon_{r,ref}} = 1 - \frac{\hat{\varepsilon}_r}{\hat{\sigma}^2} \tag{A3}$$

ACKNOWLEDGMENT

The authors would like to thank Kento Nishibayashi in Chiba University for experimental support.

REFERENCES

[1] T. Arai *et al.*, "Noninvasive measurement of alkaline phosphatase activity in embryoid bodies and coculture spheroids with scanning electrochemical microscopy," *Anal. Chem.*, vol. 85, no. 20, pp. 9647–9654, 2013, doi: 10.1021/ac401824q.

[2] J. L. Connell, J. Kim, J. B. Shear, A. J. Bard, and M. Whiteley, "Real-time monitoring of quorum sensing in 3D-printed bacterial aggregates using scanning electrochemical microscopy," *Proc. Nat. Acad. Sci. USA*, vol. 111, no. 51, pp. 18255–18260, 2014, doi: 10.1073/pnas.1421211111.

[3] T.-E. Lin, S. Rapino, H. H. Girault, and A. Lesch, "Electrochemical imaging of cells and tissues," *Chem. Sci.*, vol. 9, no. 20, pp. 4546–4554, 2018, doi: 10.1039/c8 sc01035 h.

[4] K. Y. Inoue *et al.*, "Advanced LSI-based amperometric sensor array with light-shielding structure for effective removal of photocurrent and mode selectable function for individual operation of 400 electrodes," *Lab Chip*, vol. 15, no. 3, pp. 848–856, 2015, doi: 10.1039/c4lc01099j.

[5] Y. Kanno *et al.*, "Electrochemicolor imaging using an LSI-based device for multiplexed cell assays," *Anal. Chem.*, vol. 89, no. 23, pp. 12778–12786, 2017, doi: 10.1021/acs.analchem.7b03042.

[6] J. Yao and M. Takei, "Application of process tomography to multiphase flow measurement in industrial and biomedical fields: A review," *IEEE Sensors J.*, vol. 17, no. 24, pp. 8196–8205, Dec. 2017, doi: 10.1109/JSEN.2017.2682929.

[7] X. Liu, J. Yao, T. Zhao, H. Obara, Y. Cui, and M. Takei, "Image reconstruction under contact impedance effect in micro electrical impedance tomography sensors," *IEEE Trans. Biomed. Circuits Syst.*, vol. 12, no. 3, pp. 623–631, Jun. 2018, doi: 10.1109/TBCAS.2018.2816946.

[8] T. Sun, S. Tsuda, K.-P. Zauner, and H. Morgan, "On-chip electrical impedance tomography for imaging biological cells," *Biosens. Bioelectron.*, vol. 25, no. 5, pp. 1109–1115, 2010, doi: 10.1016/j.bios.2009.09.036.

[9] Y. Yang, J. Jia, S. Smith, N. Jamil, W. Gamal, and P.-O. Bagnaninchi, "A miniature electrical impedance tomography sensor and 3-D image reconstruction for cell imaging," *IEEE Sensors J.*, vol. 17, no. 2, pp. 514–523, Jan. 2017, doi: 10.1109/JSEN.2016.2631263.

[10] J. Li, D. Kikuchi, A. Sapkota, and M. Takei, "Quantitative evaluation of electrical parameters influenced by blood flow rate with multiple-frequency measurement based on modified Hanai mixture formula," *Sens. Actuat. B, Chem.*, vol. 268, pp. 7–14, Sep. 2018, doi: 10.1016/j.snb.2018.04.077.

[11] X. Liu, Y. Cui, T. Zhao, D. Kawashima, H. Obara, and M. Takei, "Quantitative detection of living yeast fraction from mixed living and dead cell solution by micro electrical impedance spectroscopy," *IEEE Access*, vol. 7, pp. 33970–33977, 2019, doi: 10.1109/ACCESS.2019.2902576.

[12] D. Kawashima, S. Li, H. Obara, and M. Takei, "Low-frequency impedance-based cell discrimination considering ion transport model in cell suspension," *IEEE Trans. Biomed. Eng.*, vol. 68, no. 3, pp. 1015–1023, Mar. 2021.

[13] E. Malone, G. S. dos Santos, D. Holder, and S. Arridge, "Multifrequency electrical impedance tomography using spectral constraints," *IEEE Trans. Med. Imag.*, vol. 33, no. 2, pp. 340–350, Feb. 2014, doi: 10.1109/TMI.2013.2284966.

[14] N. Goren *et al.*, "Multi-frequency electrical impedance tomography and neuroimaging data in stroke patients," *Sci. Data*, vol. 5, pp. 1–10, Jul. 2018, doi: 10.1038/sdata.2018.112.

[15] H. Ammari, L. Giovangigli, L. H. Nguyen, and J.-K. Seo, "Admittivity imaging from multi-frequency micro-electrical impedance tomography," *J. Math. Anal. Appl.*, vol. 449, no. 2, pp. 1601–1618, 2017, doi: 10.1016/j.jmaa.2017.01.004.

[16] M. R. Baidillah, D. Kawashima, and M. Takei, "Compensation of volatile-distributed current due to variance of the unknown contact impedance in an electrical impedance tomography sensor," *Meas. Sci. Technol.*, vol. 30, no. 3, 2019, Art. no. 34002, doi: 10.1088/1361-6501/aafb22.

[17] S. C. Jun, J. Kuen, J. Lee, E. J. Woo, D. Holder, and J. K. Seo, "Frequency-difference EIT (fdEIT) using weighted difference and equivalent homogeneous admittivity: Validation by simulation and tank experiment," *Physiol. Meas.*, vol. 30, no. 10, pp. 1087–1099, 2009, doi: 10.1088/0967-3334/30/10/009.

[18] J. Kuen, E. J. Woo, and J. K. Seo, "Multi-frequency time-difference complex conductivity imaging of canine and human lungs using the KHU mark1 EIT system," *Phys. Meas.*, vol. 30, no. 6, p. S149, 2009, doi: 10.1088/0967-3334/30/6/S10.

[19] T. I. Oh *et al.*, "Validation of a multi-frequency electrical impedance tomography (mfEIT) system KHU Mark1: Impedance spectroscopy and time-difference imaging," *Physiol. Meas.*, vol. 29, no. 3, pp. 295–307, 2008, doi: 10.1088/0967-3334/29/3/002.

[20] I. E. Frank and J. H. Friedman, "A statistical view of some chemometrics regression tools," *Technometrics*, vol. 35, no. 2, pp. 109–135, 1993.

[21] D. Bertsimas, A. King, and R. Mazumder, "Best subset selection via a modern optimization lens," 2015, *arXiv:1507.03133*.

[22] R. A. Ghunem, K. Assaleh, and A. H. El-Hag, "Artificial neural networks with stepwise regression for predicting transformer oil furan content," *IEEE Trans. Dielectr. Electr. Insul.*, vol. 19, no. 2, pp. 414–420, Apr. 2012, doi: 10.1109/TDEI.2012.6180233.

[23] T. Hastie, R. Tibshirani, and J. Friedman, *The Elements of Statistical Learning Data Mining, Inference, and Prediction* (Springer Series in Statistics), 1 st ed. New York, NY, USA: Springer, 2001.

[24] T. J. Archdeacon, *Correlation and Regression Analysis: A Historian's Guide*. Madison, WI, USA: Univ. Wisconsin Press, 1994.

[25] N. R. Draper and H. Smith, *Applied Regression Analysis*, vol. 326. New York, NY, USA: Wiley, 1998.

[26] W. Q. Yang and S. Liu, "Electrical capacitance tomography with a square sensor," in *Proc. 1 st World Congr. Ind. Process. Tomogr.*, 1999, pp. 313–317.

[27] D. S. Holder, *Electrical Impedance Tomography: Methods, History, and Applications*, 1 st ed. Boca Raton, FL, USA: CRC Press, 2005.

[28] M. Takei and Y. Saito, "Application of the generalized vector sampled pattern matching method to reconstruction of electrical capacitance CT images," *Meas. Sci. Technol.*, vol. 15, no. 7, pp. 1371–1381, 2004, doi: 10.1088/0957-0233/15/7/021.

[29] D. Cadena-Herrera *et al.*, "Validation of three viable-cell counting methods: Manual, semi-automated, and automated," *Biotechnol. Rep.*, vol. 7, pp. 9–16, Sep. 2015, doi: 10.1016/j.btre.2015.04.004.

[30] H. P. Schwan, "Electrical properties of tissue and cell suspensions," *Adv. Biol. Med. Phys.*, vol. 5, pp. 147–209, Jan. 1957, doi: 10.1016/b978-1-4832-3111-2.50008-0.